



Fast single metal cation conduction in ion-water aggregated aqueous battery electrolytes

Received: 7 October 2024

Accepted: 7 May 2025

Published online: 16 May 2025

Chen Xu^{1,3}, Huijian Wang^{1,3}, Chengjun Lei^{1,3} , Jinye Li¹, Wenjiao Ma¹ & Xiao Liang^{1,2} ✉

Metal ion transport in solution is closely linked to its interactions with counter anions and solvent molecules. This interplay creates a longstanding trade-off between transference number (tM^{n+}), ionic conductivity (δ), and solvation process. Advanced aqueous batteries with metal negative electrode require electrolytes with unity tM^{n+} , high δ and low solvation energy. Here we introduce guanidinium sulfate (Gdm_2SO_4) into metal sulfate aqueous solutions to construct the ion-water aggregated electrolytes. These electrolytes exhibit fast single ion conduction, approaching unity tM^{n+} and high δ over 50 mS cm^{-1} for various metal cations ($M = \text{Zn, Cu, Fe, Sn and Li}$). The ion-water aggregates, dynamically formed by strong hydrogen bonding between sulfate anions, guanidinium cations and water, featuring an unfrustrated topological structure to suppress both anion mobility and water activity. This general configuration decouples the metal charge carrier from its coordination sheath, resulting in decreased solvation energy. These merits lead to homogeneous metal plating/stripping behavior with high coulombic efficiency of 99.9%. Moreover, the ion-water aggregates with reinforced kosmotropic characteristics significantly decrease the freezing point of the sulfate-based electrolytes to -28°C , making them widely applicable in aqueous metal batteries for both intercalation and conversion positive electrodes.

Ion transport within electrolytes facilitates simultaneous electrochemical reactions at both positive and negative electrodes, forming the foundational principle of secondary batteries^{1,2}. The transference number of an electrolyte typically denotes the fraction of total electric current carried by cations (tM^{n+}), while ionic conductivity (δ) reflects the overall movement of charge carriers, including both cations and anions³. These movements predominantly occur within the bulk liquid, but dynamics alter sharply at the electrode interface, where (de)solvation constitutes a critical event for electrochemical reactions^{4,5}. These properties inherently reflect the electrolyte solution structure, collectively influencing battery performance metrics.

Electrolytes exhibiting single ion conduction (tM^{n+} approaching unity) and high δ present attractive prospects for achieving dendrite-free metal negative electrodes with high specific capacities^{6,7}. Although the dendritic growth on different metal negative electrodes is characterized by their respective nucleation/growth kinetics, Chazalviel's model suggests electrolytes with high tM^{n+} and δ correspond to a longer Sand's time to slow down the dendrite nucleation kinetics⁸. Moreover, high tM^{n+} suppresses interfacial electric fields generated by cation depletion, ensuring uniform ion distribution, and enhancing electrode kinetics^{9,10}. This forms the basis for developing solid electrolytes with unity tLi^+ in Li metal batteries, despite encountering

¹State Key Laboratory of Chem/Bio-Sensing and Chemometrics, Joint International Research Laboratory of Energy Electrochemistry, College of Chemistry and Chemical Engineering, Hunan University, Changsha 410082, China. ²Greater Bay Area Institute for Innovation, Hunan University, Guangzhou 511340, China.

³These authors contributed equally: Chen Xu, Huijian Wang, Chengjun Lei. ✉e-mail: xliang@hnu.edu.cn

critical interfacial challenges¹¹. Nonetheless, liquid electrolytes with salt concentrations of 1–2 M typically exhibit tM^{n+} of 0.2–0.4 and δ around 10^{-3} – 10^{-2} S cm⁻¹, regardless of whether they are aqueous or nonaqueous and their cation types^{12,13}.

Compared to organic solvents used in lithium-ion battery (LIB) electrolytes, water offers lower viscosity and high dielectric constant, enhancing its effectiveness as a plasticizer for rapid ion transport^{14,15}. However, achieving concomitantly high tM^{n+} and δ in aqueous electrolytes remains challenging. In dilute, fully dissociated binary salt solutions in water, both cations and anions are mobile, theoretically yielding a transference number of 0.5. Yet, extensive cation hydration reduces tM^{n+} to approximately 0.2 (Fig. 1a)^{12,13}. Immobilizing counter anions in gel electrolytes can approach near-unity tM^{n+} , however, polymer chain entanglement limits their ionic conductivity (Fig. 1b)^{6,7}. Increasing salt concentration to enter the “water-in-salt” regime, such as acetates^{16,17}, chlorides^{18,19}, or bis(trifluoromethylsulfonyl) imide (TFSI)^{20,21}, significantly enhances charge carrier populations. However, the prevalence of contact ion pairs can adversely affect tM^{n+} , δ , and desolvation kinetics simultaneously (Fig. 1c), despite the electrochemical window of the electrolyte could be expanded. In particular, in frequently used highly concentrated ZnCl₂ aqueous electrolytes, intensive Zn²⁺-Cl⁻ interactions assemble an ionic network compromising both tZn^{2+} and δ ²². These challenges provide valuable inspiration for the innovative electrolyte design strategies that enable the formation of “free” cations in liquid electrolyte by solvation manipulation.

Here, the guanidinium sulfate (Gdm₂SO₄) is introduced into metal sulfate electrolytes to construct ion-water aggregates, principally disrupting the traditional trade-off relations between tM^{n+} , δ and the solvation energy in aqueous electrolytes, realizing fast single ion conduction for various metal cations (Fig. 1d). Gdm₂SO₄ is an inexpensive industrial chemical with high water solubility, chemical stability, and forms near neutral aqueous solution. It facilitates ion-water aggregation due to dynamic and strong hydrogen bonding between sulfate anions, guanidinium cations and water, decoupling of them from the metal charge carrier, thus resulting in fast single ion conduction, weakened solvation energy and suppressed dendrite growth on metal negative electrodes. The previously established ion

aggregation structure of Gdm₂SO₄ solution with protein denaturant properties provides a critical foundation for our design of ion-water aggregated electrolyte system²³. Moreover, it substantially lowers the freezing point of the sulfate-based electrolytes, exhibiting wide application in aqueous metal batteries.

Results

Ion-water aggregation

The guanidinium moiety, like the aromatic benzene ring, has conjugated p-orbitals filled with six electrons, forming a non-cyclic, closely conjugated system with unique Y-aromaticity²⁴. This π -conjugated structure indicates it is highly stable and basic in aqueous solution. A solution of 1 m Gdm₂SO₄ has a pH of 7, in contrast to the acidic nature of typical metal sulfate solutions (pH < 5). The symmetric tetrahedral structure of sulfate ions allows them to form double hydrogen bonds with multiple guanidinium cations in nearly ideal linear geometrical configurations due to spacing matching²⁵. While both groups involved in the hydrogen bonding interaction are charged, it leads to higher energy hydrogen bonds compared to conventional hydrogen bonding in bulk water²³. Such strong hetero ion pairing between guanidinium and sulfate leads to ion aggregation^{26,27}, while the remaining O in sulfate anion provides hydrogen bonding acceptor to interacting with H₂O. DFT calculation shows the local electronic structures and charge transfers of ion aggregate of guanidinium, sulfate, and water (Fig. 1e). Previous molecular dynamics (MD) simulations even suggest that these ion aggregates extend to nanometer scale^{23,28}. However, accurate measurements of ion aggregates in solution remains challenging²⁹, with the size of ion aggregates being controversial according to varying interpretations from neutron diffraction²⁸ and dielectric relaxation spectroscopy³⁰. Normal metal sulfate salts used in aqueous batteries, such as ZnSO₄ (denoted as Zn), SnSO₄ (Sn), FeSO₄ (Fe), CuSO₄ (Cu), and Li₂SO₄ (Li), were individually blended with Gdm₂SO₄ (GS) in different molar ratios to form the ion-water aggregated aqueous electrolytes (Supplementary Fig. 4). Supplementary Table 1 shows the number of molecules in zinc electrolytes based on the composition ratio.

The ion aggregation in Gdm₂SO₄ solutions is evidenced by the concentration-dependent shifting of the ν -SO₄²⁻ Raman band

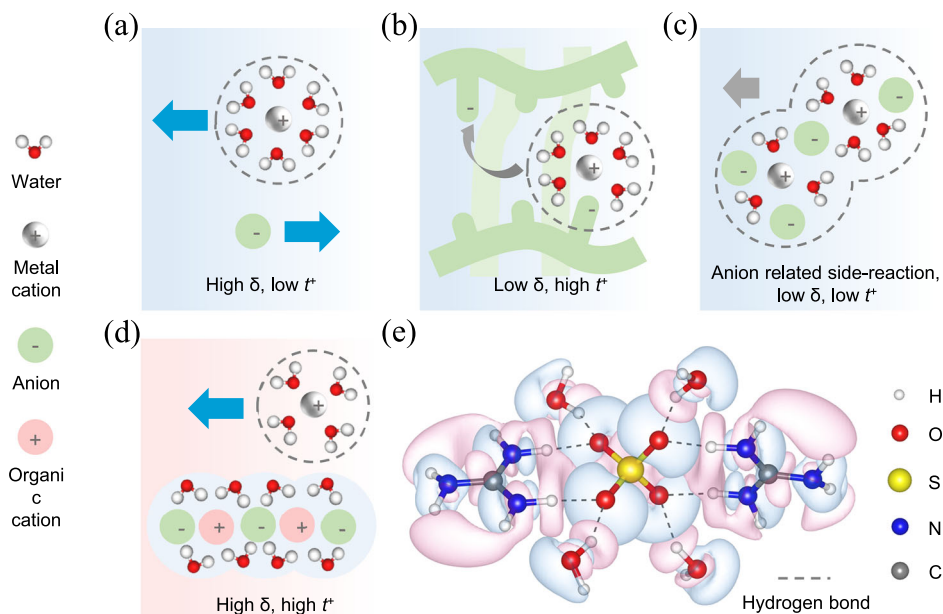


Fig. 1 | Schematic demonstration of ion migration in various electrolytes. a The conventional dilute electrolyte, **(b)** polymer gel electrolyte, **(c)** “water-in-salts” electrolyte, and **(d)** ion-water aggregated electrolyte; **e** the unfrustrated topological

structure of the hydrogen bonding between guanidinium, sulfate, and water and their differential charge densities. Light blue and pink represent the gain and loss of electrons, respectively.

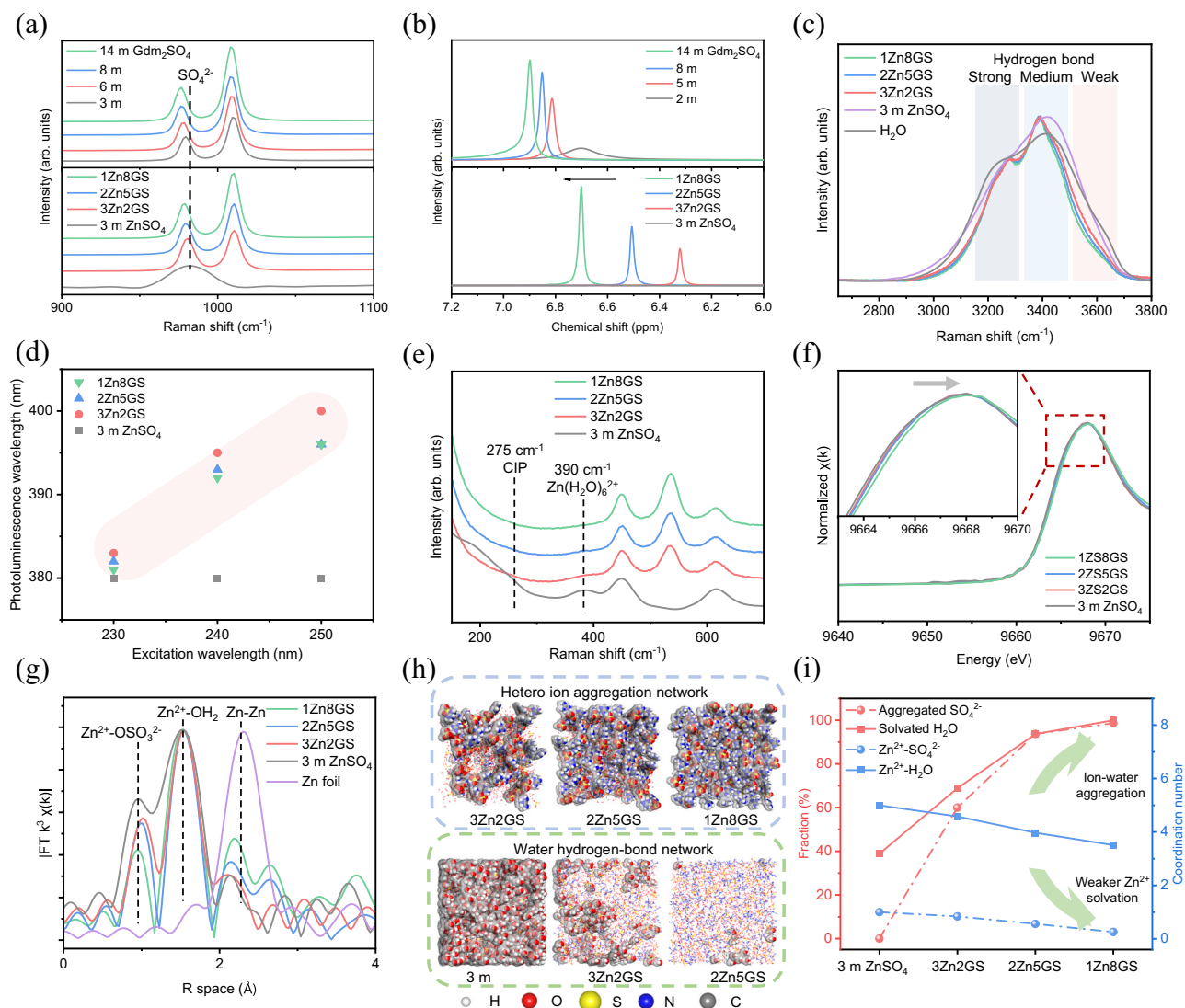


Fig. 2 | Investigation of the ion-water aggregates and detailed electrolyte composition are recorded in Supplementary Table 1. **a** Raman spectra of ν -SO $_4^{2-}$ band in different electrolytes; **b** ^1H NMR spectrum of the characteristic peak of the guanidinium; **c** Raman spectra of the O-H stretching region of the water; **d** The variation of the photoluminescence peak position with the change in excitation

wavelength; **e** Raman spectra of Zn $^{2+}$ solvation in various electrolytes; **f** Zn K-edge XANES and **(g)** EXAFS spectra in R space of different electrolytes; **h** Snapshots of hetero-ion aggregation and water hydrogen-bond networks in 3 m ZnSO $_4$ and ion-water aggregated electrolytes; **i** Evolution of the fractions of aggregated SO $_4^{2-}$, solvated H $_2$ O, and Zn $^{2+}$ coordination number in different electrolytes.

(symmetric stretching mode) to a lower frequency (Fig. 2a), attributed to the inductive effect of hydrogen donating guanidinium³¹. The similar shift observed in ZnSO $_4$ -Gdm $_2$ SO $_4$ electrolytes suggests that guanidinium captures sulfate from the Zn $^{2+}$ solvation sheath, reinforcing ion aggregation on the guanidinium coordination center. Such ν -SO $_4^{2-}$ band differs from the solvent separated ion pair (SSIP) or contacted ion pair (CIP) presented in ZnSO $_4$ solution, which blue shifted at high concentrations³². Additionally, the ^1H nuclear magnetic resonance (NMR) characteristic peak of guanidinium shifted to the low field (Fig. 2b), indicating abundant hydrogen bonding between guanidinium and sulfate in both concentrated Gdm $_2$ SO $_4$ solutions and ion-aggregated electrolytes.

Since guanidinium cannot saturate the hydrogen bonds of the sulfate oxygen atoms, the ion aggregates provide hydrogen-bonding acceptors for incorporating water. The O-H stretching region of the water in ZnSO $_4$ and ZnSO $_4$ -Gdm $_2$ SO $_4$ electrolytes demonstrates specific strong and medium hydrogen bonding induced by Gdm $_2$ SO $_4$, which interrupt the intramolecular hydrogen bonds of bulk water (Fig. 2c). Such O-H stretching mode is similar to that of concentrated

Gdm $_2$ SO $_4$ solution (Supplementary Fig. 5a). In contrast, in guanidinium chloride or guanidinium thiocyanate solutions, the Raman bands of O-H stretching vibration show a significant blue shift, attributed to the hydration of guanidinium cation to form abundant weak hydrogen bonds (Supplementary Fig. 5b)^{26,27}. These results illustrate the solvation structure in the ZnSO $_4$ -Gdm $_2$ SO $_4$ electrolyte, where sulfate assembles guanidinium and water into ion-water aggregates. The structural heterogeneity of aggregates in these electrolytes is further supported by their unusual photoluminescence property (Fig. 2d). In contrast to ZnSO $_4$ electrolyte, the photoluminescence peak of these ion-water aggregated electrolytes red-shifts along with increasing the excitation wavelength (Supplementary Fig. 6), violating Kasha's rule, which states that the luminescence characteristics do not depend on the excitation wavelength³³.

The strong interaction between sulfate, guanidinium, and water decouples these species from Zn $^{2+}$ sheath, reducing the coordination of water and sulfate with Zn $^{2+}$. The Raman band at 390 cm $^{-1}$, attributed to zinc hexahydrate (Zn(H $_2$ O) $_6^{2+}$), gradually disappears with increasing Gdm $_2$ SO $_4$ content, and the zinc-sulfate-H $_2$ O CIP (Zn $^{2+}$ SO $_4^{2-}$ (H $_2$ O) $_5$) at

275 cm^{-1} also vanishes (Fig. 2e). Supplementary Fig. 7 shows the Raman spectra of tin sulfate, copper sulfate, ferrous sulfate, lithium sulfate, and their ion-water aggregated electrolytes. Due to decoupling of ion-water aggregation from the metal charge carriers, these ion-water aggregated electrolytes show a very similar pattern in the Raman spectra, demonstrating the characteristic red-shift of sulfate and the absence of metal cation hydrates. The vibrational peak of hydrated iron at 390 cm^{-1} diminishes in the ion-water aggregated electrolyte³⁴. Notably, Sn^{2+} is prone to hydrolysis and precipitate as basic tin sulfate ($\text{Sn}_x\text{SO}_4(\text{OH})_y$) in water, necessitating the blending with strong acids (H_2SO_4) to realize a 0.2 m solubility for battery application³⁵. However, the acidic environment intensifies hydrogen evolution reaction on tin negative electrodes³⁶. The ion-water aggregation unexpectedly inhibits the hydrolysis of Sn^{2+} , allowing the dissolution of 1 m SnSO_4 , and the characteristic Sn-SO_4 peak vanished in ion-water aggregated electrolyte³⁷.

The solvation structure of the ion-water aggregated electrolytes was also studied by X-ray absorption near edge structure (XANES) and X-ray absorption fine structure (EXAFS) at the metal *K*-edge. Compared with blank ZnSO_4 electrolyte, the $\text{ZnSO}_4\text{-Gdm}_2\text{SO}_4$ electrolytes exhibit higher Zn *K*-edge energy in the XANES spectrum (Fig. 2f). It suggests fewer electron-donating groups residing in the Zn^{2+} solvation sheath, opposing to the conventional concentrated electrolyte, such as 20 m ZnCl_2 (Supplementary Fig. 8a, b), which exhibits a lower edge energy due to pronounced enrichment of anions and H_2O in the form of $[\text{ZnCl}_{2+x}(\text{H}_2\text{O})_y]^{x-}$ hydration networks^{17,18,22}. The $\text{Zn}^{2+}\text{-H}_2\text{O}$ coordination (1.5 Å) normalized Fourier transformation of EXAFS reveals the reduced $\text{Zn}^{2+}\text{-SO}_4^{2-}$ coordination (1.0 Å) in *R* space (Fig. 2g), despite SO_4^{2-} anion concentration is greatly elevated in the ion-water aggregated electrolytes, indicating a less hydrated and anion coordinated Zn^{2+} solvation sheath due to ion-water aggregation. XANES and EXAFS measurements at the *K*-edge of Cu and Fe also show the elevated edge energy, weakened $\text{M}^{2+}\text{-SO}_4^{2-}$ and $\text{M}^{2+}\text{-H}_2\text{O}$ coordination (Supplementary Fig. 8c–f), verifying the general feasibility of the ion-water aggregation strategy.

MD simulations were conducted to verify the solvation environment of the ion-water aggregated electrolytes, highlighting the evolution of ion aggregation and water hydrogen-bond networks (Fig. 2h). In 3 $\text{Zn}2\text{GS}$ electrolyte, ions begin to aggregate, forming an ionic network structure and becomes fully intertwined in the 2 $\text{Zn}5\text{GS}$ and 1 $\text{Zn}8\text{GS}$ electrolytes. The presence of ion aggregation between guanidinium and sulfate significantly disrupts the hydrogen-bond network of bulk water, with merely intramolecular or ion-dipole hydrogen-bond network being observed in 1 $\text{Zn}8\text{GS}$ electrolyte. The radial distribution functions and coordination number also provide the fractions of aggregated sulfate, water and the Zn^{2+} hydration sheath (Fig. 2i and Supplementary Note 1), which are consistent with proposed solution structure. The ion-water aggregates not only alter the water hydrogen bond network but also weaken the solvation of metal ions, markedly differing from the conventional sulfate-based electrolytes or the water-in-salt electrolytes.

The properties of ion-water aggregated electrolytes

In the ion-water aggregated electrolyte, anions are immobilized in the ion-water aggregates, ensuring a high transference number for the charge carriers (metal cations). The transference number of Zn^{2+} , Cu^{2+} , Fe^{2+} , Sn^{2+} , and Li^+ are 0.95, 0.88, 0.86, 0.96, and 0.98 in the ion-water aggregated electrolytes, respectively, far surpassing those of their corresponding blank electrolytes (Fig. 3a and Supplementary Figs. 9 and 10). The $t_{\text{Zn}^{2+}}$ is only 0.09 in a conventional “water in salt” electrolyte (20 m ZnCl_2 , Supplementary Fig. 10f), and 0.32 in 1 m ZnSO_4 electrolyte. MD simulations were performed to investigate the mass transfer characteristics in the ion-water aggregated electrolyte (Supplementary Note 2). The $t_{\text{Zn}^{2+}}$ was calculated along with the relevant contributions from other ions. For the 3 $\text{Zn}2\text{GS}$ solution, $t_{\text{Zn}^{2+}}$ was determined to be 0.6, with SO_4^{2-} contributing about 20%. In

contrast, for the 1 $\text{Zn}8\text{GS}$ solution, $t_{\text{Zn}^{2+}}$ increased to 0.87, while the contribution of SO_4^{2-} was negligible, indicating that sulfate ions are immobilized within the aggregates. The ionic conductivity of the $\text{ZnSO}_4\text{-Gdm}_2\text{SO}_4$ electrolyte is rationally increased with the elevated GS/ZnSO_4 ratios (Supplementary Fig. 11a). The ion-water aggregated electrolytes of Cu^{2+} , Fe^{2+} , Sn^{2+} , and Li^+ also demonstrated high ionic conductivities of 59.6, 44.6, 60.4, 32.8, and 54.3 mS cm^{-1} , which are higher than those of their corresponding blank electrolyte, except for the case of 3 m H_2SO_4 + 0.2 m SnSO_4 electrolyte (Supplementary Fig. 11b). This is attributed the 5 to 10 times equivalent conductance of H^+ in the acidic solution than metal cations³⁸. To further understand the electrochemical properties of these electrolytes in a wider temperature range, the ionic conductivities were supplemented from -20 to $+60$ °C, demonstrating consistent pattern in the comparison between ion-water aggregated electrolyte and blank electrolyte (Supplementary Fig. 12). Considering the transference number of these electrolytes, the ion-water aggregated electrolytes exhibit superior high effective cation ionic conductivity (δM^{+}) compared to the blank electrolytes (Fig. 3b).

The solvation energy of Zn^{2+} was calculated based on their distinct solvation structures. As the Gdm_2SO_4 concentration increased, a notable reduction in solvation energy was observed, decreasing from 367.2 kcal mol^{-1} in 3 m ZnSO_4 to 348.9 kcal mol^{-1} in 1 $\text{Zn}8\text{GS}$ (Fig. 3c). Moreover, the solvation energy can be quantitatively or qualitatively assessed by measuring the open circuit potential of symmetrical cells with different coordination environments^{39,40}. Ion-water aggregated electrolytes induce substantial shifts in stabilized potential compared to their corresponding blank electrolytes (Fig. 3d), indicating weakened solvation of metal cations due to ion-water aggregation.

The electrochemical window of the ion-water aggregated electrolytes was demonstrated by 1 $\text{Mg}8\text{GS}$ solution to exclude metal deposition before hydrogen evolution. Comparing 1 m MgSO_4 with 1 $\text{Mg}8\text{GS}$, the hydrogen evolution potential shifted from -0.96 to -1.35 V vs. the saturated calomel electrode (SCE), and the oxygen evolution potential elevated from 0.98 to 1.15 V (Fig. 3e), indicating that the ion-water aggregation broadened the electrochemical window of the electrolyte. This is attributed to the enhanced hetero hydrogen bonding of water in the ion-water aggregates. The hydrogen atoms in water, observed by ^1H NMR, shifted to a higher field with increasing Gdm_2SO_4 concentration, indicating the strengthened chemical bonding in water (Fig. 3f). The enhanced hydrogen bonding is also responsible for the available protons in the electrolyte, as determined by pH value. The 3 m ZnSO_4 solution has a pH of 3.8, whereas the pH of ion-water aggregated electrolyte increased to 5.3 (Fig. 3g), significantly reducing the proton concentration in the electrolyte to exclude hydrogen evolution upon metal plating. As a result, parasitic reactions occur on metal negative electrodes could be suppressed, as demonstrated by investigation of Zn corrosion reactions in these electrolytes (Supplementary Note 3).

According to the Hofmeister series, the highly symmetric sulfate anion with high charge density is strongly kosmotropic, while trifluoromethanesulfonate (OTf^-) is a typical chaotropic anion due to low symmetry and large charge delocalization (Supplementary Fig. 13a)^{41,42}. Kosmotropic anions form strong hydrogen bonds with water, typically promoting a hydrogen bonding network that elevates the freezing point of the electrolyte⁴². In accordance, at -5 °C, 3 m ZnSO_4 electrolyte froze while 3 m $\text{Zn}(\text{OTf})_2$ electrolyte remained fluid (Supplementary Fig. 13b). In contrast, these ion-water aggregated electrolytes did not freeze at -5 °C and prevented the heptahydrate ZnSO_4 precipitation. Differential scanning calorimetry (DSC) showed that the freezing points of 3 m ZnSO_4 and 3 $\text{Zn}2\text{GS}$ electrolytes were similar to pure water. As the concentration of Gdm_2SO_4 increased, the freezing point of 2 $\text{Zn}5\text{GS}$ and 1 $\text{Zn}8\text{GS}$ electrolytes decreased to -19.3 °C and -28.1 °C (Fig. 3h), respectively, meeting the practical requirements for zinc metal batteries in cold weather.

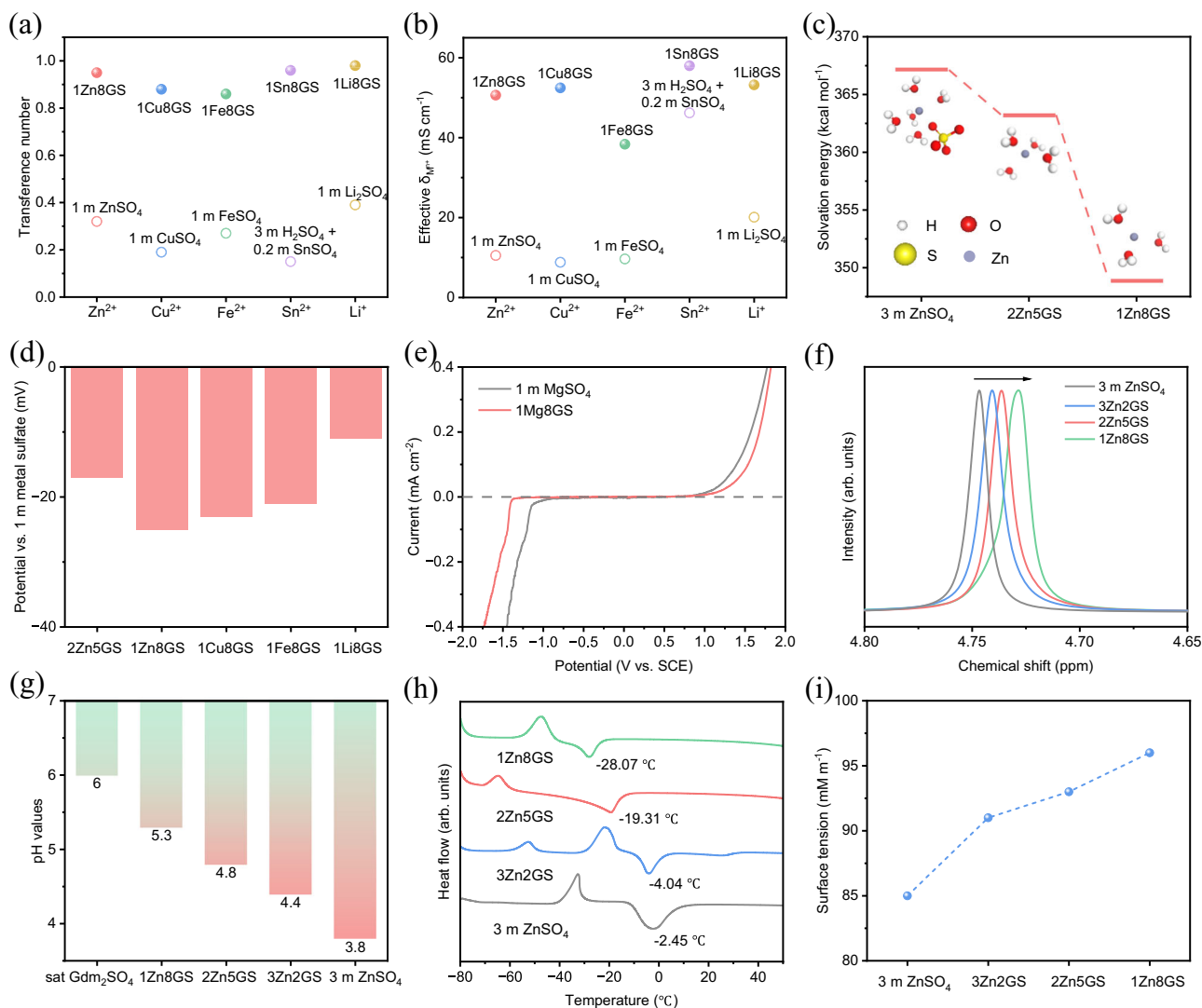


Fig. 3 | The physicochemical properties of the ion-water aggregated electrolyte. **a** Metal cation transference number and **(b)** effective δM^+ of various electrolytes; **c** Solvation energy of different electrolytes calculated from the statistical solvation structures. Insets are the representative solvation configurations; **d** the open circuit potential in cells with Zn||Zn, Cu||Cu, Fe||Fe and lithium iron phosphate||lithium iron phosphate (LFP)||LFP symmetric electrodes and asymmetric

electrolytes; **e** Linear scanning voltammetry (LSV) curves of the ion-water aggregated electrolytes and blank electrolytes; **f** ^1H chemical shifts of water in different electrolytes and corresponding electrolytes composition are recorded in Supplementary Table 1; **g** pH value of 3 m ZnSO_4 and ion-water aggregated electrolytes; **h** DSC analysis and **(i)** surface tension of ZnSO_4 and ion-water aggregated electrolytes. The surface tension was determined by the pendant-drop method.

The kosmotropic/chaotropic properties are strongly correlated with the surface tension of the electrolyte, where the hydration of kosmotropic anion increases surface tension⁴³. As the Gdm_2SO_4 content increased, the electrolytes exhibited higher surface tension, confirming the kosmotropic nature of the ion-water aggregates (Fig. 3i). It promotes the construction of a structured water environment and enhance the salting-out effect, thereby reducing the solubility of organic solutes⁴⁴. It is showed that the $\text{Zn}(\text{OTf})_2$ electrolyte is miscible with polyethylene glycol 400 (PEG400), whereas self-stratification was observed in ZnSO_4 electrolyte and ion-water aggregated electrolytes due to their strong salting-out effect (Supplementary Fig. 14). Moreover, ion-water aggregated electrolytes improve the wettability towards zinc metal, as demonstrated by the decreased contact angle (Supplementary Fig. 15).

Metal plating/stripping

The initial nucleation potential of metal electrodeposit in various electrolytes was determined by the chronopotentiometry method. As shown in Fig. 4a, the 3 m ZnSO_4 electrolyte exhibited an

overpotential of 41 mV at a current density of 1 mA cm^{-2} , whereas the ion-water aggregated electrolytes showed higher overpotential, suggesting higher nucleation resistance. This could be attributed to the adsorption of ion aggregates on the Zn metal surface compared with water molecules, constructing a water-poor electric double layer (EDL)⁴⁵. The EDL structure change is evidenced by the shifted Zeta potential (Supplementary Fig. 16) and the decreased contact angle between Zn and electrolytes (Supplementary Fig. 15)⁴⁶. Such electron enriched EDL will slow the plating rate of fast-moving cations and inhibit rampant dendrite growth⁴⁷. In the chronoamperometry tests, the current density of the 3 m ZnSO_4 electrolyte gradually increased over time, demonstrating the redundant two-dimensional diffusion process caused by the increase of effective surface area of zinc negative electrode (dendrite) during the nucleation process⁴⁸. The current in the ion-water aggregated electrolyte stabilized after 200 s, suggesting a restricted two-dimensional diffusion behavior. Besides, Cu^{2+} , Fe^{2+} , and Sn^{2+} demonstrated similar nucleation behavior in ion-water aggregated electrolytes (Supplementary Fig. 17).

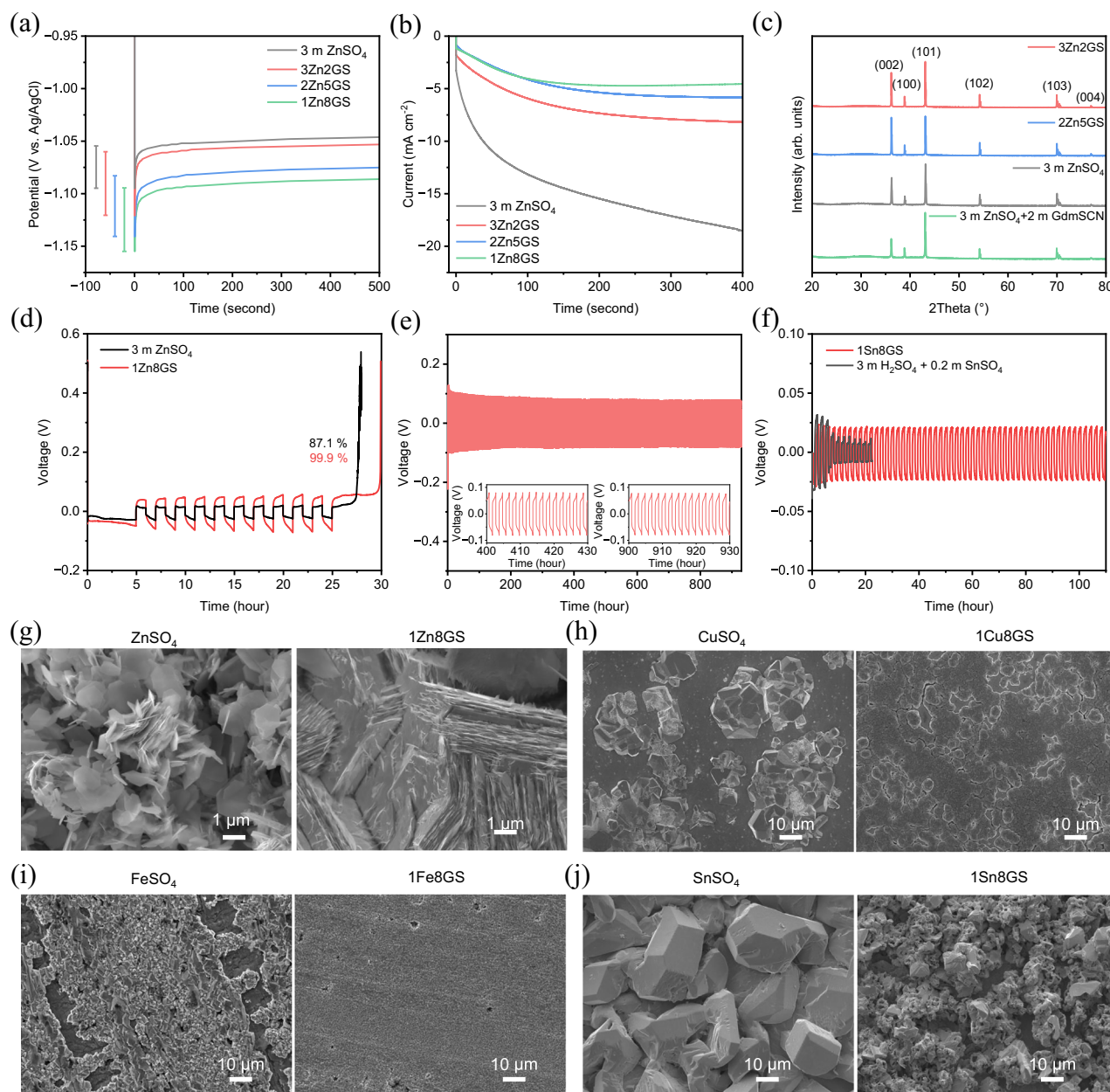


Fig. 4 | Investigation of metal plating/stripping behavior. **a** Chronopotentiometry curves of Zn electrode in blank and ion-water aggregated electrolytes at 1 mA cm^{-2} and corresponding electrolytes composition are recorded in Supplementary Table 1; **b** Chronoamperometry curves of Zn electrode with a fixed potential of 150 mV; **c** XRD patterns of zinc after plating/stripping in different electrolytes; **d** Coulombic efficiency of Zn-Ti cell in 3 m ZnSO_4 and ion-water aggregated electrolytes based on Aurbach

method, where the charge/discharge current at 2 mA cm^{-2} , the capacity of plating is 10 mAh cm^{-2} and cycling number is 10; Long-term plating/stripping tests for (e) Zn||Zn and (f) Sn||Sn cells in ion aggregated electrolytes at 2 mA cm^{-2} and 2 mAh cm^{-2} ; SEM images of various metals after 10th plating/stripping in blank and ion-water aggregated electrolytes: **g** Zn, **h** Cu, **i** Fe, and (j) Sn.

Benefiting from the elevated nuclear barrier in the ion-water aggregated electrolytes, the nucleus radius decrease, which is conducive to the controlled and uniform growth of zinc (Fig. 4b)⁴⁶. This promotes more homogeneous and dense plating and inhibits zinc dendrites growth. The facets orientation of zinc negative electrode after 10 cycles of plating/stripping at 1 mA cm^{-2} and 1 mAh cm^{-2} was evaluated by XRD (Fig. 4c), verifying a significantly enhanced Zn (002) facet orientation in the ion-water aggregated electrolytes, while the (101) plane orientation was preferred in the control electrolyte. The coulombic efficiency (CE) of Zn||Ti cells was tested using the Aurbach method⁴⁹, where Ti counter electrode provides a harsh environment due to its low affinity and inert nature. The CE in 1Zn8GS, 2Zn5GS, and 3Zn2GS electrolytes were 99.9%, 99.9%, and 99.8%, respectively

(Fig. 4d and Supplementary Fig. 18a, b), far surpassing that in 3 m ZnSO_4 (87.1%, Fig. 4d). Long-term cycling performance of the Zn||Ti cells were carried out at 2 mA cm^{-2} and 2 mAh cm^{-2} (Supplementary Fig. 19). The 2Zn5GS and 3Zn2GS electrolytes showed long-term cycling stability of more than 1000 h with high CE, while that in 3 m ZnSO_4 electrolyte suffered short circuit in 30 h. Beyond zinc metal, plating/stripping tests of Cu, Sn, Fe metal on Ti or Cu counter electrode also demonstrated elevated coulombic efficiency and prolonged cycling life (Supplementary Figs. 20 and 21).

Zn||Zn symmetric cells in 1Zn8GS, 2Zn5GS, and 3Zn2GS electrolytes cycled stably without abnormal voltage fluctuation for the test times of 900, 2200, and 1300 h at 2 mA cm^{-2} and 2 mAh cm^{-2} , respectively (Fig. 4e and Supplementary Fig. 22a, b). In contrast, the cell in the

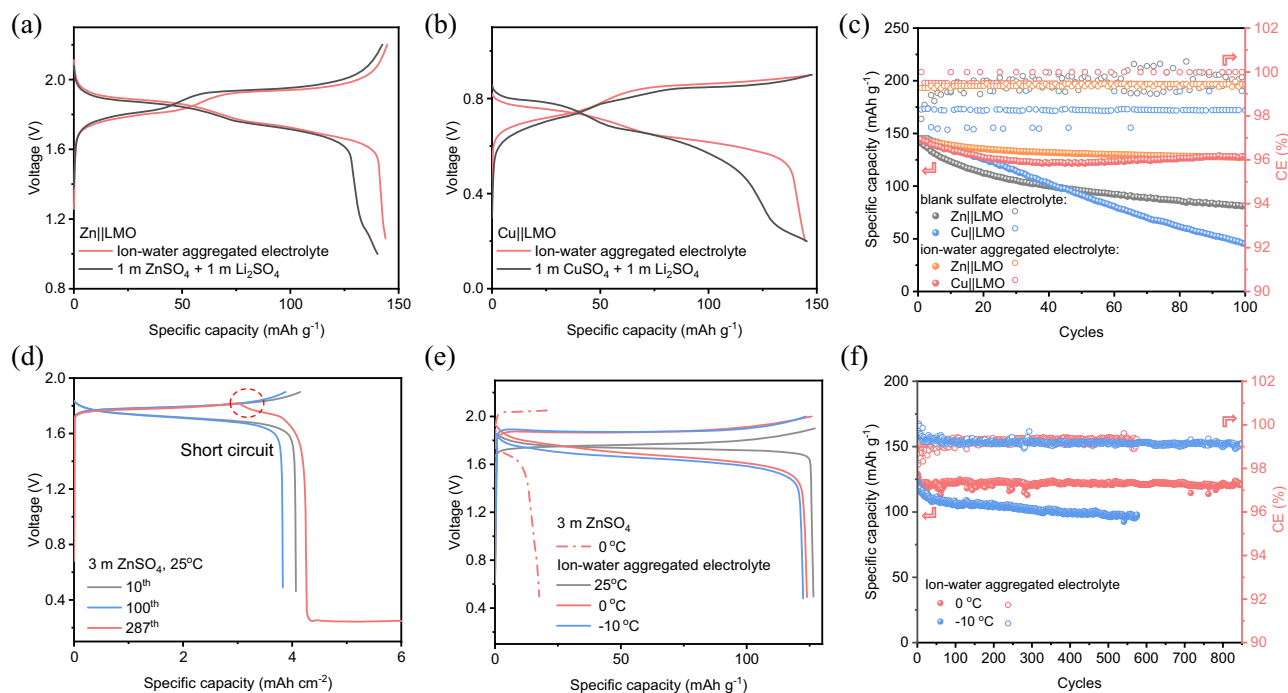


Fig. 5 | The full cell performances. Voltage profiles of (a) Zn||LMO and (b) Cu||LMO batteries in various electrolytes at 148 mA g⁻¹; c Cycling performance of Zn||LMO and Cu||LMO batteries; d Cycling performance of Zn||Br static, batteries in 3 m ZnSO₄ at 110 mA g⁻¹; e Voltage profiles of Zn||Br static battery in 3 m ZnSO₄ and ion-

water aggregated electrolyte at different temperature at 55 mA g⁻¹; f Cycling performance of Zn||Br static batteries in ion-water aggregated electrolyte at low temperatures.

3 m ZnSO₄ electrolyte experienced a steep voltage drop below 5 mV after only 110 h of cycling, indicating a short circuit. Notably, the symmetric cell exhibited a shorter cycle life in the ZnSO₄ electrolyte with guanidinium thiocyanate (Supplementary Fig. 22c). The long-term stability of symmetrical cells of Cu, Sn, Fe metal in corresponding ion-water aggregated electrolyte were extended significantly (Fig. 4f and Supplementary Fig. 23). Particularly, Sn is poorly reversible in conventional 3 m H₂SO₄ + 0.2 m SnSO₄ electrolyte, however, the 1Sn8GS electrolyte sustains long-term stability for Sn plating/stripping.

The Zn electroplating event was monitored by in situ optical microscopy (Supplementary Fig. 24). At a current density of 5 mA cm⁻², prominent zinc dendrite growth was observed on the zinc negative electrode after 30 min of electroplating in 3 m ZnSO₄, forming loose and uneven protrusions with significant hydrogen evolution. Benefiting from the optimized Zn plating behavior and suppressed water activity in ion-water aggregated electrolytes, homogenous electroplating was achieved. The ion-water aggregated electrolytes significantly inhibit dendrite growth and hydrogen evolution on the negative electrode, resulting in uniform electroplating with high areal capacity up to 10 mAh cm⁻².

Figure 4g shows the SEM images of the zinc negative electrode after 10 cycles in 3 m ZnSO₄ and ion-water aggregated electrolytes, respectively. Zinc negative electrode turned into rough and uneven after cycling in 3 m ZnSO₄ electrolyte, with corrosion-induced concave structures and vertical flakes. The addition of guanidinium thiocyanate in to ZnSO₄ electrolyte did not improve the flatness of zinc surface, resulting in loose and mossy plating (Supplementary Fig. 25). In contrast, zinc negative electrode in the ion-water aggregated electrolytes remained relatively homogeneous and flat, with the plating morphology mainly consisting of tightly stacked hexagonal Zn(002) facets. In analog, for Cu, Sn, and Fe metal negative electrode, the blank electrolytes lead to non-uniform plating and large particle sizes (Fig. 4h-j). Conversely, ion-water aggregated electrolytes promote metal nucleation, resulting in smaller deposit size and more compact morphology.

Aqueous metal batteries

The advances of the ion-water aggregated electrolytes were validated in metal negative electrode based full batteries by pairing with intercalation and conversion type positive electrode. LiMn₂O₄ (LMO) was selected as the intercalation positive electrode option, due to its high voltage and stability in aqueous batteries⁵⁰. Double metal cation electrolytes were prepared, in which Li₂SO₄ is responsible for positive electrode chemistry and the other metal sulfate accomplishes the metal electroplating on anode. While the charge carriers are decoupled from the ion-water aggregates, we speculate a similar solvation structure in these double metal electrolytes. Benefiting from the improved reversibility of metal negative electrode and unimpeded solvation in ion-water aggregated electrolytes, both Zn||LMO and Cu||LMO dual ion batteries exhibited low polarization and stable capacity over cycling at 148 mA g⁻¹ (Fig. 5a, b). In contrast, batteries with sulfate electrolytes showed rapid capacity decay with larger polarization (Fig. 5c).

The energy dense Br electrode was selected as the conversion type positive electrode by pairing with Zn anode to construct the static Zn||Br battery. Hexylpyridinium bromide (HPY Br) was blended with ZnBr₂ to accomplish Br⁻/Br⁰ redox couple (see Methods for details), which possess high complexation strength with polybromide⁴⁴. The kosmotropic characteristic of the ion-water aggregated electrolytes provide the salting-out ability to synergistically inhibit the shuttling and hydrolysis of polybromides complexes. At room temperature, the batteries using ion-water aggregated electrolytes exhibited low voltage polarization at 110 mA g⁻¹, achieving high areal capacities of 5 mAh cm⁻² (Supplementary Fig. 26a). The battery demonstrates outstanding capacity retention of 88.1% after 600 cycles (Supplementary Fig. 26b), whereas in 3 m ZnSO₄ electrolyte the battery experiences a short circuit after 287 cycles (Fig. 5d and Supplementary Fig. 27). At 0 °C and -10 °C, the Zn||Br batteries in ion-water aggregated electrolyte achieved high reversible capacities of 124 and 122 mAh g⁻¹ at 55 mA g⁻¹, respectively, which are close to the room temperature capacity, indicating a high utilization of active materials at low

temperature (Fig. 5e). In contrast, the ZnSO_4 electrolyte froze at 0°C , resulting in failure of the $\text{Zn}||\text{Br}$ batteries. The $\text{Zn}||\text{Br}$ batteries showed good cycling stability at low temperatures in the ion-water aggregated electrolytes, retaining 96.8% capacity over 800 cycles at 0°C (Fig. 5f). The improved cycling stability at low temperatures could also be attributed to the improved Zn negative electrode stability in ion-water aggregated electrolyte at low temperatures, as shown by the long-term plating/stripping of $\text{Zn}||\text{Zn}$ symmetric cell at -20°C (Supplementary Fig. 28). These results confirm the excellent low-temperature performance of $\text{Zn}||\text{Br}$ static batteries with ion-water aggregated electrolytes, extending the operating temperature window of conventional ZnSO_4 electrolytes.

High temperatures can exacerbate possible side reactions and aqueous electrolyte evaporation. $\text{Zn}||\text{Br}$ batteries with a positive electrode areal loading of 1.5 mAh cm^{-2} were tested at 45°C . The $\text{Zn}||\text{Br}$ battery using ion-water aggregated electrolyte retained 88.1% capacity after 6000 cycles at 657 mA g^{-1} , while it only retained 48.7% in 3 M ZnSO_4 electrolyte after 2000 cycles (Supplementary Fig. 29). These highlight the promising application of the ion-water aggregated electrolyte in practical $\text{Zn}||\text{Br}$ batteries.

Discussion

We declare a versatile approach of controlling the electrolyte solvation structure by establishing an ion-water aggregation, sustaining fast single ion conduction approaching unity tM^{n+} and high ionic conductivity over 50 mS cm^{-1} for various metal cations ($M = \text{Zn}, \text{Cu}, \text{Fe}, \text{Sn}$ and Li). This is achieved by blending the corresponding metal sulfates aqueous solution with a chemical-stable guanidinium sulfate salt. Comprehensive investigations suggest the ion-water aggregates are dynamically formed by strong hydrogen bonding between sulfate anions, guanidinium cations and water, featuring an unfrustrated topological structure to suppress both anion mobility and water activity. This general configuration decouples the metal charge carrier from its coordination sheath, resulting in decreased solvation energy. Benefiting from the advantages of ion-water aggregated electrolyte, uniform and stable metal plating/stripping was achieved with high coulombic efficiency up to 99.9%.

Other merits of the ion-water aggregated electrolytes include the decreased melting point and enhanced kosmotropic characteristics. While frequently used sulfate aqueous electrolytes for metal batteries get frozen near 0°C , such ion-water aggregated formula extends it down to -28°C , providing a wider operational temperature in aqueous metal batteries with both intercalation and conversion positive electrode. The reinforced kosmotropic characteristic of the ion-water aggregated electrolyte respect to the normal sulfate electrolyte, on the other hand, literally enhances the “salting-out” effect to mitigates the dissolution of active materials from the positive electrode, i.e., the polybromine complexes used in this work for static $\text{Zn}||\text{Br}$ batteries. Long term cycling performance was achieved for the static $\text{Zn}||\text{Br}$ batteries at both low temperatures and high temperatures. Ion-water aggregated electrolytes with alternative guanidinium structures such bicyclic guanidinium and poly-guanidinium are currently being investigated in our laboratory to establish some general design principle. The understanding of this ion-water aggregates will undoubtedly benefit the future efforts of seeking improved electrochemical storage devices.

Methods

Materials

All chemicals were purchased from Shanghai Aladdin Biochemical Technology Co. without any special annotations and were used as received. The 0.01 mm thickness zinc, 0.1 mm thickness copper, 0.1 mm thickness iron, and tin foil (0.01 mm thickness, 99.99%, Hebei Qingyuan Technology Co.) were cleaned with ethanol and subsequently used as metal electrodes without additional polishing

treatment. Glass fiber (Whatman GF/A, 12 mm in diameter) was used as the separator for the cells.

Preparation of electrolytes and electrodes

All aqueous electrolytes are prepared according to the molality concentration by dissolving a certain molar amount of salt solute in one kilogram of water (mol kg^{-1}), and the concentration is unified to be “m”.

LMO electrode: 80 wt% LiMn_2O_4 (DoDoChem), 10 wt% super P (Shenzhen Kejing MATERIALS Technology Co.), and 10 wt% polyvinylidene fluoride (PVDF, Kejing MATERIALS Technology Co.) were blended with N-Methylpyrrolidone (NMP, AR). The slurry was casted onto the Al foil, followed by vacuum drying at 60°C for 24 h. The active material loaded foil was rolled and sliced with a diameter of 10 mm . The areal loading of LiMn_2O_4 is about 5 mg cm^{-2} .

Br electrode: hexylpyridinium bromide (HPYBr) was prepared by the halogenation reaction of pyridine with bromohexane¹. HPYBr- ZnBr_2 slurry was prepared by mixing 37 wt% HPYBr, 37 wt% ZnBr_2 , 20 wt% Super P carbon, 6 wt% sodium carboxymethylcellulose (CMC) binder with water. The slurry was transferred into a $10 \times 8\text{ cm}^2$ polytetrafluoroethylene mold and flattened by gravity, followed by vacuum drying at 60°C for 24 h. The areal loading of the electrode could be controlled by the slurry mass for each mold. The positive electrodes were sliced into disk with a diameter of 12 mm .

AC electrode: the active carbon electrode used for Linear scanning voltammetry (LSV) study was prepared according to the similar procedure by blending 90 wt% active carbon (Aladdin), 10 wt% PVDF, and NMP into the slurry. The slurry was casted onto Ti foil followed by vacuum drying.

Physicochemical characterizations

The morphology of the zinc negative electrode was investigated using a Hitachi-S4800 scanning electron microscope. The pH of the electrolyte was determined using a FiveEasy Plus pH meter. Photoluminescence of electrolytes was carried out on a Hitachi F-7000 fluorescence spectrophotometer. Chemical environment of water molecules and organic molecules were determined by NMR analysis (Bruker Ascend HD 400 MHz). Raman spectra were obtained on an InVia Reflex with a laser wavelength of 532 nm . X-ray absorption near edge structure (XANES) spectra of the Zn, Cu, Fe K-edge for anion-water aggregated electrolytes, sulfate-based blank electrolytes, and metal foil references were collected at RapidXAFS 1 M (Anhui Absorption Spectroscopy Analysis Instrument Co., Ltd.) by transmission mode at 20 kV and 40 mA . The collected data were processed with the ATHENA module. The X-ray absorption fine structure (XAFS) spectra were Fourier-transformed in the R space to obtain a radial distribution function. The contact angle and surface tension of the electrolyte were accessed on a KRÜSS DSA100 video optical contact angle measuring instrument. Differential scanning calorimetry (DSC) was conducted on TA DSCQ10 to evaluate the freezing point of the electrolytes. X-ray diffraction (XRD) was tested on Bruker D8 Advance. The Scanning electron microscope (SEM, JSM-7610FPlus) was applied for morphological characterization and Energy dispersive spectroscopy (EDS, ULTIM MAX 40, $0\text{--}20\text{ keV}$) element mapping was performed for elements analysis.

Computation

The detailed computation methods could be found in Supplementary Information and the VESTA software is employed to visualize the crystal structures and charge density difference maps in this paper (Fig. 1e).⁵¹

Electrochemical tests

All electrochemical studies were conducted in Swagelok-type cells with titanium rod current collectors. The electrolyte volume for each cell was $80\text{ }\mu\text{L}$. The battery was assembled by simply stacking the electrodes and the wetted separators layer by layer. Galvanostatically charge/discharge

tests were performed on Neware Battery Test System (CT-4008T, Shenzhen, China). For Zn||LMO batteries, the charge and discharge cut-off voltages were set from 1 V to 2.2 V for 1 M ZnSO₄ + 1 M Li₂SO₄ and from 1.1 V to 2.2 V for ion-water aggregated electrolyte, respectively. For Cu||LMO batteries, the charge and discharge cut-off voltages were set from 0.2 V to 0.9 V. For Zn||Br batteries, the charge and discharge cut-off voltages in 3 M ZnSO₄ were set from 0.5 V to 1.9 V and 0.5 V to 2.05 V at 0 °C and 25 °C, respectively, while from 0.5 V to 1.9 V at 25 °C and 0.5 V to 2.0 V at 0 °C, −10 °C in ion-water aggregated electrolyte. The metal plating/stripping coulombic efficiency were evaluated by a modified Aurbach method^{5,6}, where the charge/discharge current = 2 mA cm^{−2}, $Q_{\text{plating}} = 10 \text{ mAh cm}^{-2}$, and $n = 10$.

LSV, chronoamperometry, chronopotentiometry, electrochemical impedance spectroscopy (EIS), and linear polarization tests were conducted on a Gamry electrochemical workstation. EIS tests were conducted with amplitude of 0.01 V and frequency from 0.1 Hz to 1×10^6 Hz. The ionic conductivity of the electrolyte system was determined by the following equation:

$$\delta = \frac{d}{R_b S} \quad (1)$$

The electrochemical stability windows of the electrolytes were evaluated using LSV on active carbon electrodes (25 mg cm^{−2}) with a scanning rate of 0.2 mV s^{−1}. Ion transference number ($t_{\text{Zn}^{2+}}$, $t_{\text{Cu}^{2+}}$, $t_{\text{Fe}^{2+}}$, $t_{\text{Sn}^{2+}}$, and $t_{\text{Li}^{+}}$) was measured with combination measurements of alternating current impedance and direct current polarization using the symmetric cells, respectively⁷. The transference number of Li⁺ was specifically accessed with a lithium iron phosphate (LFP) symmetric battery⁸. The LFP electrodes were pre-charged in a beaker cell filled with 5 ml of 1 M Li₂SO₄, and an active carbon electrode was used as the counter electrode, utilizing a capacity cutoff to reach 50% depth of discharge (DOD). The symmetric cells underwent a short circuit before the measurements to fully equilibrate the potentials of two electrodes. The polarization currents of cell including initial (I_0) and steady-state (I_{ss}) were recorded under a direct polarization voltage, which ranging from 10 to 30 mV depending on their response current. The interfacial resistances before (R_0) and after (R_{ss}) polarization were tested by EIS. Afterwards, ion transference number was calculated from Bruce-Vincent-Evans Equation⁹:

$$t = \frac{I_{ss}(\Delta V - I_0 R_0)}{I_0(\Delta V - I_{ss} R_{ss})} \quad (2)$$

In situ observation of zinc electrodeposition was conducted in a simple homemade quartz cell. Two zinc foils with an area of $4 \times 0.5 \text{ cm}^2$ were fixed on the inner wall of the quartz cell and placed vertically under the optical lens. The electrodeposition experiments were carried out at a current density of 5 mA cm^{−2} and optical micrographs of the zinc foil were taken at regular intervals. The coulombic efficiency is calculated as the ratio of discharge capacity divided by the charge capacity in the preceding charge cycle.

Data availability

The authors declare that all the relevant data are available within the paper and its Supplementary Information file or from the corresponding author on request. The DFT calculations structure of ion aggregate of guanidinium, sulfate, and water are recorded in Supplementary Data 1. Source data are provided with this paper.

References

- Liang, Y. & Yao, Y. Designing modern aqueous batteries. *Nat. Rev. Mater.* **8**, 109–122 (2022).
- Li, M., Wang, C., Chen, Z., Xu, K. & Lu, J. New concepts in electrolytes. *Chem. Rev.* **120**, 6783–6819 (2020).
- Xu, K. Nonaqueous liquid electrolytes for lithium-based rechargeable batteries. *Chem. Rev.* **104**, 4303–4418 (2004).
- Ma, W. et al. Tailoring desolvation strategies for aqueous zinc-ion batteries. *Energy Environ. Sci.* **17**, 4819–4846 (2024).
- Kundu, D. et al. Aqueous vs. nonaqueous Zn-ion batteries: consequences of the desolvation penalty at the interface. *Energy Environ. Sci.* **11**, 881–892 (2018).
- Shan, X. et al. A polymer electrolyte with high cationic transport number for safe and stable solid Li-metal batteries. *ACS Energy Lett.* **7**, 4342–4351 (2022).
- Dong, J. et al. Spontaneous molecule aggregation for nearly single-ion conducting sol electrolyte to advanced aqueous zinc metal batteries: the case of tetraphenylporphyrin. *Angew. Chem. Int. Ed.* **63**, e202401441 (2024).
- Yang, J.-L., Yang, P., Xiao, T. & Fan, H. J. Designing single-ion conductive electrolytes for aqueous zinc batteries. *Matter* **7**, 1928–1949 (2024).
- Yang, Q. et al. Dendrites in Zn-based batteries. *Adv. Mater.* **32**, 2001854 (2020).
- Bai, P., Li, J., Brushett, F. R. & Bazant, M. Z. Transition of lithium growth mechanisms in liquid electrolytes. *Energy Environ. Sci.* **9**, 3221–3229 (2016).
- Bachman, J. C. et al. Inorganic solid-state electrolytes for lithium batteries: mechanisms and properties governing ion conduction. *Chem. Rev.* **116**, 140–162 (2016).
- Diederichsen, K. M., McShane, E. J. & McCloskey, B. D. Promising routes to a high Li⁺ transference number electrolyte for lithium ion batteries. *ACS Energy Lett.* **2**, 2563–2575 (2017).
- Purser, E. P. & Stokes, R. H. Transference numbers in aqueous solutions of zinc sulfate. *J. Am. Chem. Soc.* **73**, 5650–5652 (1951).
- Wang, F. et al. Hybrid aqueous/non-aqueous electrolyte for safe and high-energy Li-ion batteries. *Joule* **2**, 927–937 (2018).
- Xu, J. et al. Aqueous electrolyte design for super-stable 2.5 V LiMn₂O₄ || Li₄Ti₅O₁₂ pouch cells. *Nat. Energy* **7**, 186–193 (2022).
- Cai, S. et al. Water–salt oligomers enable supersoluble electrolytes for high-performance aqueous batteries. *Adv. Mater.* **33**, 2007470 (2021).
- Dong, D., Wang, T., Sun, Y., Fan, J. & Lu, Y.-C. Hydrotropic solubilization of zinc acetates for sustainable aqueous battery electrolytes. *Nat. Sustain.* **6**, 1474–1484 (2023).
- Zhang, Q. et al. Modulating electrolyte structure for ultralow temperature aqueous zinc batteries. *Nat. Commun.* **11**, 4463 (2020).
- Wu, X. et al. Reverse dual-ion battery via a ZnCl₂ water-in-salt electrolyte. *J. Am. Chem. Soc.* **141**, 6338–6344 (2019).
- Wang, F. et al. Highly reversible zinc metal anode for aqueous batteries. *Nat. Mater.* **17**, 543–549 (2018).
- Brown, J. et al. A guanidium salt as a chaotropic agent for aqueous battery electrolytes. *Chem. Commun.* **59**, 12266–12269 (2023).
- Ji, X. A perspective of ZnCl₂ electrolytes: the physical and electrochemical properties. *eScience* **1**, 99–107 (2021).
- Mason, P. E., Dempsey, C. E., Neilson, G. W. & Brady, J. W. Nanometer-scale ion aggregates in aqueous electrolyte solutions: guanidinium sulfate and guanidinium thiocyanate. *J. Phys. Chem. B* **109**, 24185–24196 (2005).
- Blanco, F., Kelly, B., Alkorta, I., Rozas, I. & Elguero, J. Cation–π interactions: complexes of guanidinium and simple aromatic systems. *Chem. Phys. Lett.* **511**, 129–134 (2011).
- Gao, B. & Liu, Z. A first principles study on the solvation and structure of SO₄^{2−}(H₂O)_n, n=6–12. *J. Chem. Phys.* **121**, 8299–8306 (2004).
- Dempsey, C. E., Mason, P. E., Brady, J. W. & Neilson, G. W. The reversal by sulfate of the denaturant activity of guanidinium. *J. Am. Chem. Soc.* **129**, 15895–15902 (2007).
- Graziano, G. Contrasting the denaturing effect of guanidinium chloride with the stabilizing effect of guanidinium sulfate. *Phys. Chem. Chem. Phys.* **13**, 12008 (2011).

28. Mason, P. E., Neilson, G. W., Kline, S. R., Dempsey, C. E. & Brady, J. W. Nanometer-scale ion aggregates in aqueous electrolyte solutions: guanidinium carbonate. *J. Phys. Chem. B* **110**, 13477–13483 (2006).
29. Hunger, J., Neueder, R., Buchner, R. & Apelblat, A. A conductance study of guanidinium chloride, thiocyanate, sulfate, and carbonate in dilute aqueous solutions: ion-association and carbonate hydrolysis effects. *J. Phys. Chem. B* **117**, 615–622 (2013).
30. Hunger, J., Niedermayer, S., Buchner, R. & Hefter, G. Are nanoscale ion aggregates present in aqueous solutions of guanidinium salts? *J. Phys. Chem. B* **114**, 13617–13627 (2010).
31. Ben Mabrouk, K., Kauffmann, T. H., Aroui, H. & Fontana, M. D. Raman study of cation effect on sulfate vibration modes in solid state and in aqueous solutions. *J. Raman Spectrosc.* **44**, 1603–1608 (2013).
32. Yang, H. et al. A metal–organic framework as a multifunctional ionic sieve membrane for long-life aqueous zinc–iodide batteries. *Adv. Mater.* **32**, 2004240 (2020).
33. Biswas, B. & Singh, P. C. The unusual visible fluorescence violating the Kasha's rule suggests the aggregation of guanidinium carbonate in its aqueous medium. *J. Mol. Liq.* **253**, 211–216 (2018).
34. Kanno, H. & Hiraishi, J. A Raman study of aqueous solutions of ferric nitrate, ferrous chloride and ferric chloride in the glassy state. *J. Raman Spectrosc.* **12**, 224–227 (1982).
35. Zhang, H. et al. A high-capacity Sn metal anode for aqueous acidic batteries. *Joule* **7**, 971–985 (2023).
36. Yu, Z. et al. Highly reversible tin redox chemistry for stable anode-free acidic proton battery. *Joule* **8**, 1063–1079 (2024).
37. Holze, R. & Bittins-Cattaneo, B. The oxidation state of upd-tin on a platinum electrode studied with surface raman spectroscopy. *Electrochim. Acta* **33**, 353–358 (1988).
38. Majima, H., Peters, E., Awakura, Y. & Park, S. K. Electrical conductivity of acidic sulfate solution. *Met. Trans. B* **18**, 41–47 (1987).
39. Kim, S. C. et al. Potentiometric measurement to probe solvation energy and its correlation to lithium battery cyclability. *J. Am. Chem. Soc.* **143**, 10301–10308 (2021).
40. Fan, H. et al. Tailoring interfacial Zn²⁺ coordination via a robust cation conductive film enables high performance zinc metal battery. *Energy Storage Mater.* **49**, 380–389 (2022).
41. Huang, S., Hou, L., Li, T., Jiao, Y. & Wu, P. Antifreezing hydrogel electrolyte with ternary hydrogen bonding for high-performance zinc-ion batteries. *Adv. Mater.* **34**, 2110140 (2022).
42. Zhang, Q. et al. Chaotropic anion and fast-kinetics cathode enabling low-temperature aqueous Zn batteries. *ACS Energy Lett.* **6**, 2704–2712 (2021).
43. Dos Santos, A. P., Diehl, A. & Levin, Y. Surface tensions, surface potentials, and the hofmeister series of electrolyte solutions. *Langmuir* **26**, 10778–10783 (2010).
44. Xu, C. et al. Practical high-energy aqueous zinc-bromine static batteries enabled by synergistic exclusion-complexation chemistry. *Joule* **8**, 461–481 (2024).
45. Lv, Y. et al. Engineering a self-adaptive electric double layer on both electrodes for high-performance zinc metal batteries. *Energy Environ. Sci.* **15**, 4748–4760 (2022).
46. Huang, C. et al. Stabilizing zinc anodes by regulating the electrical double layer with saccharin anions. *Adv. Mater.* **33**, 2100445 (2021).
47. Zhong, Y. et al. Triple-function hydrated eutectic electrolyte for enhanced aqueous zinc batteries. *Angew. Chem. Int. Ed.* **62**, e202310577 (2023).
48. Shi, M. et al. Molecule engineering of sugar derivatives as electrolyte additives for deep-reversible Zn metal anode. *Angew. Chem. Int. Ed.* **63**, e202407261 (2024).
49. Huang, Y. et al. Eco-friendly electrolytes via a robust bond design for high-energy Li metal batteries. *Energy Environ. Sci.* **15**, 4349–4361 (2022).
50. Shang, Y. et al. Long-life Zn anode enabled by low volume concentration of a benign electrolyte additive. *Adv. Funct. Mater.* **32**, 2200606 (2022).
51. Momma, K. & Izumi, F. VESTA 3 for three-dimensional visualization of crystal, volumetric and morphology data. *J. Appl. Cryst.* **44**, 1272–1276 (2011).

Acknowledgements

We acknowledge Dr. T.T.Z. from Changsha University of Science and Technology for the acquisition of XANES. X.L. appreciates the financial support from the National Key Research and Development Program of China (2019YFA0210600) (X.L.), the National Natural Science Foundation of China (22479043) (X.L.), and the Major Program of the Natural Science Foundation of Hunan Province (2021JC0006, 2025JJ30005) (X.L.).

Author contributions

X.L. and C.X. conceived and designed the study. C.X. and H.W. directed the study and contributed materials preparation and electrochemical tests. C.X., H.W., and C.L. conducted spectroscopy studies. C.L. and W.M. conducted MD simulations. C.X. and J.L. performed zinc electro-deposition and SEM studies. X.L. and C.X. contributed to data interpretation and analysis and wrote the manuscript. X.L. supervised the project. All authors contributed to the scientific discussion.

Competing interests

The authors declare no competing interests.

Additional information

Supplementary information The online version contains supplementary material available at <https://doi.org/10.1038/s41467-025-59958-x>.

Correspondence and requests for materials should be addressed to Xiao Liang.

Peer review information *Nature Communications* thanks the anonymous reviewer(s) for their contribution to the peer review of this work. A peer review file is available.

Reprints and permissions information is available at <http://www.nature.com/reprints>

Publisher's note Springer Nature remains neutral with regard to jurisdictional claims in published maps and institutional affiliations.

Open Access This article is licensed under a Creative Commons Attribution-NonCommercial-NoDerivatives 4.0 International License, which permits any non-commercial use, sharing, distribution and reproduction in any medium or format, as long as you give appropriate credit to the original author(s) and the source, provide a link to the Creative Commons licence, and indicate if you modified the licensed material. You do not have permission under this licence to share adapted material derived from this article or parts of it. The images or other third party material in this article are included in the article's Creative Commons licence, unless indicated otherwise in a credit line to the material. If material is not included in the article's Creative Commons licence and your intended use is not permitted by statutory regulation or exceeds the permitted use, you will need to obtain permission directly from the copyright holder. To view a copy of this licence, visit <http://creativecommons.org/licenses/by-nc-nd/4.0/>.

© The Author(s) 2025